

AperTO - Archivio Istituzionale Open Access dell'Università di Torino

**Laboratory scale geophysical measurements aimed at monitoring the thermal affected zone in Underground Thermal Energy Storage (UTES) applications**

**This is the author's manuscript**

*Original Citation:*

*Availability:*

This version is available <http://hdl.handle.net/2318/1558993> since 2019-01-08T11:34:23Z

*Published version:*

DOI:10.1016/j.geothermics.2016.01.011

*Terms of use:*

Open Access

Anyone can freely access the full text of works made available as "Open Access". Works made available under a Creative Commons license can be used according to the terms and conditions of said license. Use of all other works requires consent of the right holder (author or publisher) if not exempted from copyright protection by the applicable law.

(Article begins on next page)



# UNIVERSITÀ DEGLI STUDI DI TORINO

1  
2  
3  
4  
5  
6  
7  
8  
9  
10  
11  
12

***This is an author version of the contribution published on:***  
*Questa è la versione dell'autore dell'opera:*  
*[Geothermics, 61, 2016, 10.1016/j.geothermics.2016.01.011]*

***The definitive version is available at:***  
*La versione definitiva è disponibile alla URL:*  
*[<http://www.journals.elsevier.com/geothermics/>]*

13 **Laboratory scale geophysical measurements aimed at monitoring the**  
14 **thermal affected zone in Underground Thermal Energy Storage (UTES)**  
15 **applications.**

16 **N. Giordano<sup>1</sup>, C. Comina<sup>1-2</sup>, G. Mandrone<sup>1-2</sup>**

17 <sup>1</sup> Earth Science Department – Torino University (IT), Via Valperga Caluso, 35 – 10125 Torino

18 <sup>2</sup> AG3 srl – A Spin Off Company of Torino University (IT), Via Valperga Caluso, 35 – 10125 Torino

24 **Abstract**

25 Underground Thermal Energy Storage systems have showed to be a useful and increasing technical  
26 solution for covering the heating and cooling and domestic hot water buildings' demand. Thermal  
27 influence of these plants is however not still debated as it deserves and correct monitoring strategies  
28 appear to be of major importance both to better understand processes and to highlight their  
29 environmental effects into high populated areas. Litho-, hydro- and bio-sphere can indeed be adversely  
30 affected by temperature variations induced in the underground by heat storage applications. For this  
31 purpose, a geophysical approach using time-lapse electrical resistivity measurements contemporary to  
32 analogical simulations is here tested at laboratory scale. Results of the experiments are reported  
33 comparing measured apparent resistivity with direct temperature measurements and numerical  
34 simulations of heat propagation. Data presented confirmed that electrical resistivity has powerful  
35 relation with temperature variation in monitored media. In addition, they showed that also without  
36 performing data inversion valid temperature estimation can be carried out. Post processing calibration  
37 of apparent resistivity data showed to be in acceptable agreement with both temperature measurements  
38 and numerical simulations. Simple apparent electrical resistivity variations appear therefore to be a  
39 promising, economic, quick and non-invasive tool for mapping thermal modifications induced in the  
40 underground by shallow geothermal applications.

41 **Keywords:** apparent electrical resistivity; numerical simulation; analogical modeling; porous media;  
42 shallow geothermal applications.

43 **Corresponding author:**

44 Nicolò Giordano

45 nicolo.giordano@unito.it

46 Dipartimento di Scienze della Terra

47 Via Valperga Caluso, 35

48 10125 – TORINO

49 tel. +39 011 6705325

## 56 1. INTRODUCTION

57 The idea of exploiting the thermal energy provided by renewable sources has been always  
58 related to the problem that most of these sources supply energy when the user's demand is low  
59 (e.g. sun energy is related to the warm season, when the heating demand is reduced). In this  
60 respect, the thermal energy storage is a highly debated concept since the late 70s; several  
61 Underground Thermal Energy Storage (UTES) technologies have been developed in recent  
62 years to find some new solutions assuring criteria of reliability, efficiency and economic  
63 sustainability. Short-term (daily) and long-term (seasonal) storages are the two main categories  
64 discriminating the storage mechanism, depending on the duration of the storing activity. The  
65 seasonal storage seems to satisfy the annual heat demand better than the short-term, with a 60%  
66 against a 20% of total energy demand provided (Fisch et al., 1998; Sanner, 2003; Xu et al.,  
67 2014). It is however true that the seasonal storage implies bigger economical investments and  
68 wider storage volumes, hence it results in a more challenging technology in terms of storing  
69 materials, heat loss evaluations and environmental impact reductions.

70 UTES systems are based on the sensible heat storage mechanism which is considered to  
71 be a simple, low-cost, more reliable and acceptable technology compared to other alternatives  
72 (latent heat or chemical reaction/thermo-chemical sorption), even if the latter have higher  
73 energy storage densities (for detailed discussion refer to Xu et al., 2014). Several methodologies  
74 are available depending on the storing medium: (ATES – Aquifer Thermal Energy Storage)  
75 (Rosen, 1999; Paskoy et al., 2000; Dickinson et al., 2009), hot water confined in steel tanks  
76 (Novo et al., 2010; Schmidt et al., 2004) or the ground itself; in this last case the connection  
77 with the ground is provided by a series of boreholes heat exchangers (BTES – Boreholes  
78 Thermal Energy Storage) (Bakema et al., 1995; Fisch et al., 1998; Reuss et al., 2006; DLSC,  
79 2012; Giordano et al., 2016).

80 Mainly ATES and BTES have therefore geological implications. In both cases, thermal  
81 and hydrogeological properties of the ground have to be taken into account for the design and  
82 operation of the installation. Both storage systems have a strong environmental impact: a big  
83 part of the aquifer could be influenced in the first case, a noticeable underground volume is  
84 interested by drilling activity in the latter. In any case a not negligible Thermal Affected Zone  
85 (TAZ) is generated and an accurate monitoring activity must be considered to take care of the  
86 possible negative effects induced on litho-, hydro- and bio-sphere. Generally, an accurate study  
87 of the thermal behavior of the storage medium and a correct monitoring of TAZ are also useful  
88 to understand processes.

89 So far, there is limited specific knowledge about the effects of unsuitable system design  
90 (e.g. unwanted temperature and chemical changes within the subsurface and resulting  
91 consequences). Only few studies have measured the thermal effects of low enthalpy geothermal  
92 applications within field sites. Arslan and Huber (2013) compared field temperature  
93 observations with numerical simulations and laboratory measurements under a forced  
94 groundwater flow. Lo Russo et al. (2014), evidenced that the thermal plumes generated by well  
95 doublets of groundwater heat pumps can be regarded either as a potential resource or as a  
96 pollution. Bonte (2013) studied temperature-induced impacts on the groundwater quality,  
97 accounting for variations in the mobility of trace elements, redox processes and microbial  
98 communities. Most studies agree that a 10°C temperature change can be sufficient to stimulate  
99 trace elements mobility and microbial activity variations. Considering high temperature (60°C  
100 – 70°C) fluids injected in the ground by energy storage systems a potential environmental  
101 impact has therefore to be considered.

102 Classic thermal tests or monitoring strategies often rely on local and point-based  
103 measurements to monitor changes in temperature. In this context, geophysics can bring  
104 complementary information which is spatially distributed and acquired directly from the ground  
105 surface. In particular, electrical resistivity measurements could be considered as a time and  
106 cost-efficient method for monitoring shallow geothermal systems to understand thermal  
107 processes. Hermans et al. (2015) demonstrated the ability of cross-borehole time-lapse  
108 resistivity tomography to study heat flow and heat storage within a small field experiment in a  
109 shallow aquifer and Hermans et al. (2012) successfully used surface resistivity measurements  
110 to monitor temperature variations. Frangkogiannis et al. (2008) also used resistivity tomography  
111 for monitoring the thermal performance of an installed ground source heat pump system. Robert  
112 et al. (2013), under laboratory conditions, highlighted the problems of resistivity-derived  
113 temperatures owing to chemical reactions occurring both on fluid and solid phases. They  
114 observed a divergence between resistivity and temperature curves, related to decreasing  
115 solubility of some minerals (e.g. calcite precipitation) and resulting decreasing fluid  
116 conductivity with increasing temperature. A more detailed review on the use of geophysical  
117 methods to monitor temperature changes induced in the underground by shallow geothermal  
118 systems can be found in Hermans et al. (2014). More case studies are also provided by Arato et  
119 al. (2015).

120 Resistivity based measurements are potentially very powerful since useful relationships  
121 can be found in literature between temperature and electrical resistivity (Campbell, 1948; Lee  
122 and Deming, 1998; Frangkogiannis et al., 2008; Rein et al., 2004; Hayashi, 2004; Hayley et al.,  
123 2007). However, resistivity depends also in a complex way on different soil and environmental  
124 attributes. Friedman (2005) gave an overview of these parameters, and their impact, underlining  
125 three categories: (i) parameters describing the bulk soil, such as porosity ( $\Phi$ ), water content ( $\theta$ )  
126 and structure; (ii) the time-invariable solid particle quantifiers, such as particle shape and  
127 orientation, particle-size distribution, wettability or cation exchange capacity; (iii) fast-  
128 changing environmental factors, such as ionic strength, cation composition and, finally,  
129 temperature. A proper, but not easy, parameter calibration should be undertaken in order to  
130 infer relevant information such as the extension of TAZ. Devoted tests are therefore necessary  
131 in this respect. As an example, laboratory tests have the advantage that controlled boundary  
132 conditions can be obtained (parameters from the first and the second groups) such that a direct  
133 comparison of geophysical results, temperature measurements and numerical simulations can  
134 be performed. After a proper calibration it will be then possible to use electric resistivity  
135 variations with time as an imaging tool for the distribution of thermal plumes. This approach  
136 can be also profitably extended at the field scale, if some of the mentioned parameters do not  
137 change during time (particle size distribution, water content, porosity etc.).

138 The present paper therefore presents a series of laboratory tests performed on an *ad hoc*  
139 designed apparatus for testing and calibrating a methodology for monitoring the extension of  
140 TAZ caused by underground storage applications. A heat injection was induced in a porous  
141 medium and time-lapse electrical measurements were carried out together with local  
142 temperature measurements and a Finite Element Method (FEM) numerical simulation of the  
143 heat propagation. Several tests were performed by varying: porous medium, position and  
144 number of heat sources, hydraulic conditions and injection time. Resistivity and temperature  
145 measurements were then compared with numerical simulations to estimate the reliability of  
146 apparent resistivity variations in qualitatively mapping TAZ extension within the medium and  
147 in quantitatively evaluating temperature distribution within it.

148

149 **2. MATERIALS AND METHODS**

150 The proposed testing methodology consists of the following steps:

- 151 – Analogical test: heat injection and heat turnoff monitored by 4 temperature sensors
- 152 located in the medium and by hourly electrical measurements in spatial arrangement,
- 153 on two different media;
- 154 – Numerical simulations: numerical modeling of heat propagation calibrated on local
- 155 temperature measurements to extend temperature information spatially and evaluate the
- 156 eventual differences in homogeneous parameters variation;
- 157 – Resistivity data processing: calibration of the fractional change in electrical resistivity
- 158 based on the comparison with local resistivity data and temperature measurements;
- 159 – Temperature prediction and comparison: imaging of the resistivity-derived temperature
- 160 maps by means of the previous step and comparison with the numerical simulations.

161 Details on the instrumentation and procedures adopted in each step are provided in the

162 following.

163 **2.1 Laboratory apparatus and performed tests**

164 A plastic box, sized 0.8 x 0.3 x 0.3 m (**Fig. 1**), was prepared to simulate a heat injection

165 within the selected porous medium. Three sectors separated by permeable septa were

166 predisposed in order to focus the simulation in the central part of the box. In the external sectors

167 two PVC pipes, surrounded by a high porosity filling material, were placed for generating a

168 water flux by controlling the hydraulic head in the pipes. The central sector, about 0.6 m long,

169 was filled with a porous medium for 0.3 m of thickness and was equipped with 4 thermo-

170 resistances Pt100 (accuracy  $\pm 1^\circ\text{C}$ , resolution  $0.2^\circ\text{C}$ ), located at different positions depending

171 on the test, for the temperature monitoring. An electrical resistance (diameter 4 cm) and

172 powered by alternated current was used as heat source. During the tests, the source was

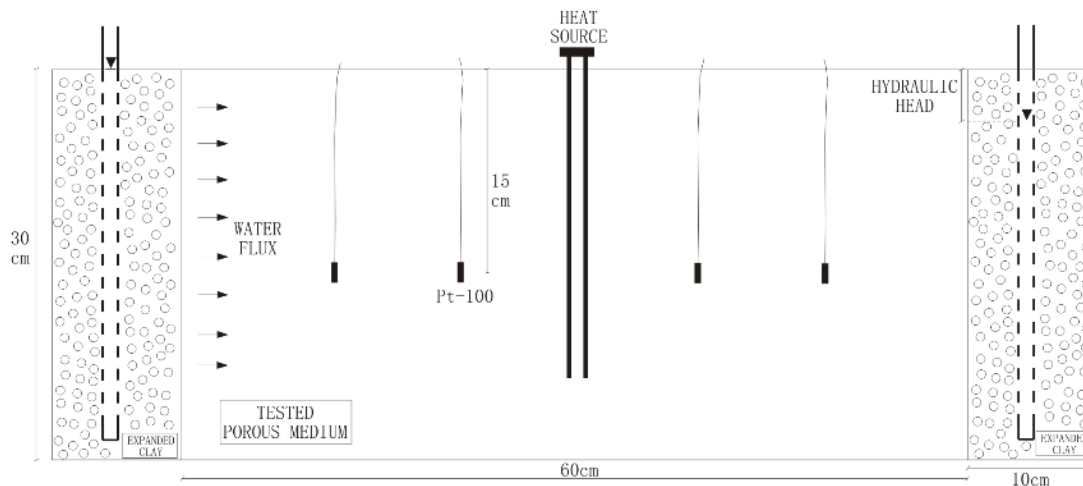
173 controlled by a thermometer and a rheostat, to assure desired constant temperature ( $60^\circ\text{C}$  for

174 all the tests). For one of the presented tests a double source has been used (**Tab. 1**). The

175 boundaries of the box were thermally insulated using cork panels and impermeable

176 membranes. A data-logger and appropriate software were used for data acquisition, in order to

177 register continuously all the controlling parameters (sampling interval 1 minute).



178

179 **Fig. 1.** Schematic depiction of the laboratory device used for the experimental tests.

180

181 **Tab. 1** – Summary of the presented tests

| Name | Porous medium | Water flux [l s <sup>-1</sup> ] | Processes               | Heat injection | Source position           |
|------|---------------|---------------------------------|-------------------------|----------------|---------------------------|
| Fs   | Fine          | -                               | Conduction              | 9 h            | 1 source central position |
| Fd   | Fine          | 1.5x10 <sup>-3</sup>            | Conduction & convection | 5 h            | 1 source central position |
| Cs   | Coarse        | -                               | Conduction              | 5 h            | 2 sources left side       |
| Cd   | Coarse        | 3.0x10 <sup>-3</sup>            | Conduction & convection | 5 h            | 1 source central position |

182

183

184

185

186

187

188

189

190

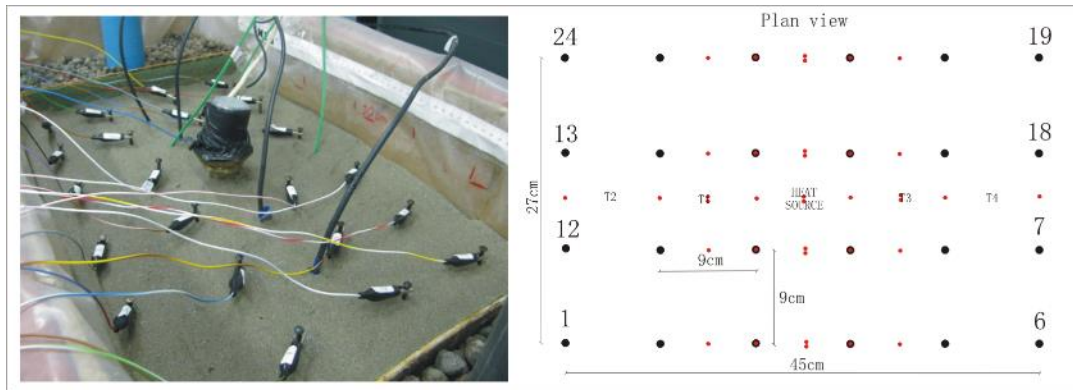
191

192

193

194

A network configuration with 24 electrodes (6 lines of 9 cm spaced electrodes) was adopted to achieve a wide spatial information around the sources (**Fig. 2**). A SYSCAL Pro multichannel georesistivitymeter was used for resistivity measurements. A short current injection time (250 ms) was adopted in order to record the set of measurements as quick as possible. A dipole - dipole array with 36 measurements (plus reciprocal, for a total of 72 measurements) was adopted. This configuration allowed us to record resistivity values roughly at the same depth of temperature sensors and to image its variation during time in a plan view around the heat source. Dipole - dipole configuration was adopted in order to improve data coverage, since number of electrodes and available space are reduced. This situation often affects also real site data, particularly in urban environment. Moreover, dipole - dipole is more prone to evaluate lateral variation in resistivity as in the case for an advancing thermal plume. Midpoints of dipole - dipole measurements are reported in red in **Fig. 2**.



195

196

197

**Fig. 2.** Electrode configuration adopted in the tests with dipole-dipole centre location (red dots on the right); the picture and the position of the temperature sensors refer to Fs test.

198

199

200

201

202

203

204

205

206

207

208

209

210

211

Two natural porous media with different grain size distributions were adopted. These materials come from two quarries nearby Torino and are therefore intended to represent typical local geological conditions of the municipality. The two media were respectively made of: (i) a fine medium with 91% wg. of sand and 9% wg. of silt, compacted at a porosity of 0.46; (ii) a coarse medium with 58% wg. of gravel (mean particle diameter  $d_0 = 5-6$  mm) and 42% wg. of sand, compacted at a porosity of 0.35. In the present paper 4 examples of several tests conducted in the box are presented (**Tab. 1**). The tests are intended to simulate the heat injection under realistic conditions; in one of the tests a double injecting source was also used. In both media a pure conduction test, with the medium completely saturated by tap water, and a conduction + convection test, where a water flux was simulated by inducing a hydraulic head gap between the two side of the box are presented. A flow rate of about  $3.0 \times 10^{-3}$  l/s of water at room temperature was induced in the coarser medium, while the flow rate adopted in the finer was about  $1.5 \times 10^{-3}$  l/s, owing to the different permeability coefficients of the tested media. The tests lasted at least 10 hours, with 5 hours of heat injection and the remaining 5 hours of cool

212 down. The electrical surveys were performed hourly from the beginning (zero condition) until  
 213 the end of the tests, when the undisturbed temperature was reached again.

## 214 2.2 Numerical simulations

215 To simulate the heat injection within the medium, the OpenGeoSys code (OGS) was  
 216 adopted (Kolditz et al., 2012). OpenGeoSys is an open-source initiative for the numerical  
 217 simulation of thermo-hydro-mechanical/chemical processes. It is a flexible FEM numerical  
 218 framework, provided to solve multifield problems in porous and fractured media for several  
 219 geological and hydrological applications. The simulations were performed using the  
 220 *heat\_transport* process for the static tests and the coupled *heat\_transport* and  
 221 *groundwater\_flow* processes for the tests simulating coupled conduction and forced convection  
 222 phenomena. The OGS governing equations for both “pure conduction” heat transport and  
 223 “conduction + convection” heat transport can be summarized in the energy balance equation,  
 224 taking into account every element of the bi-component medium (solid and water):  
 225

$$226 \gamma_b C_b \frac{\partial T}{\partial t} + \nabla q_T = Q_T \quad [1]$$

227 where at the first member the temperature ( $T$ ) variation as a function of time multiplied by  
 228 density ( $\gamma_b$ ) and specific heat capacity ( $C_b$ ) of the medium are summed to the heat flux term  $q_T$ ,  
 229 which can be divided in the two components of advective and conductive flux as follows:

$$230 q_T = \Phi \theta \gamma_w C_w v T - \lambda_b \nabla T \quad [2]$$

231 where  $\Phi$  is the porosity,  $\theta$  the water content,  $\gamma_w$  and  $C_w$  the density and the specific heat  
 232 capacity of water,  $v$  denotes Darcy velocity and  $\lambda_b$  is the bulk thermal conductivity.

233 Some preliminary evaluations comparing *ad hoc* simulations with available analytical  
 234 solutions and experimental tests were used to calibrate geometric elements, discretization mesh,  
 235 Dirichlet and Neumann boundary conditions, time step definition, medium, material and fluid  
 236 properties. The simulations were carried out setting up the same characteristics of each  
 237 experimental test performed at lab scale. A 3D model with a rectangular prism mesh of about  
 238 75,000 nodes was adopted. Lateral sides of the box were simulated as impermeable boundaries,  
 239 not allowing for heat or fluid flow and only the upper boundary was a diffusing one. The finally  
 240 adopted physical properties of the tested materials are presented in **Tab. 2**.

241 **Tab. 2** – Physical properties of the tested media adopted for numerical simulations.  
 242

|                      | $\Phi$ | $\gamma_b$<br>[t m <sup>-3</sup> ] | $k_i$<br>[m <sup>2</sup> ] | $\lambda_s$<br>[W m <sup>-1</sup> K <sup>-1</sup> ] | $\lambda_w$<br>[W m <sup>-1</sup> K <sup>-1</sup> ] | $C_s$<br>[J kg <sup>-1</sup> K <sup>-1</sup> ] | $C_w$<br>[J kg <sup>-1</sup> K <sup>-1</sup> ] | $\Delta i$<br>[m] |
|----------------------|--------|------------------------------------|----------------------------|---|---|--|--|-------------------|
| <b>Fine medium</b>   | 0.46   | 1.47                               | 1x10 <sup>-11</sup>        | 5.0   | 0.58  | 800  | 4,200  | 0.05              |
| <b>Coarse medium</b> | 0.35   | 1.72                               | 3x10 <sup>-11</sup>        | 5.0   | 0.58  | 800  | 4,200  | 0.05              |

243

244

## 245 2.3 Electrical resistivity vs. temperature

### 246 2.3.1 Adopted methodology

247 A linear dependence between temperature and electrical conductivity ( $\sigma$  – the inverse of  
248 resistivity) can be assumed in the temperature range in question (Hermans et al., 2012). Around  
249 25 °C the following relation has been proposed:

$$250 \quad \frac{\sigma_T}{\sigma_{25}} = m(T - 25) + 1 \quad [3]$$

251 where  $\sigma_T$  is the electric conductivity of the porous medium at temperature  $T$  (°C) and  $m$  is the  
252 fractional change in electrical conductivity (°C<sup>-1</sup>). A range of 0.018 °C<sup>-1</sup> and 0.025 °C<sup>-1</sup> has  
253 been found by several authors for  $m$  (Revil et al., 1998; Hayashi, 2004; Hayley et al., 2007;  
254 Hermans et al., 2012) and it varies according to the type of fluid and sediments. Water and  
255 surface conductivity effects can be separated in case of a silty or clayey medium, accounting  
256 for different fractional changes,  $m^f$  for fluid and  $m^s$  for surface conductivity. According to Revil  
257 and Linde (2006) the surface conductivity is related with the average particle diameter of the  
258 medium as follows:

$$259 \quad \sigma_S = \frac{6\Sigma_S}{d_0} \quad [4]$$

260 where  $\Sigma_S$  is the specific surface conductivity (S) and  $d_0$  is the mean particle diameter. If we  
261 reasonably assume the specific surface conductivity equal to 4.0 x 10<sup>-9</sup> S (Bolève et al., 2007),  
262 we obtain  $\sigma_S = 1.6 \times 10^{-4}$  S/m and  $\sigma_S = 9.6 \times 10^{-6}$  S/m respectively for the finer ( $d_0 = 0.15$  mm)  
263 and the coarser media ( $d_0 = 2.5$  mm). By considering that the applied tap water conductivity is  
264 5.0 x 10<sup>-2</sup> S/m, we can thus neglect the surface conductivity effect in the performed tests and  
265 assume the bulk electrical resistivity variation during the heat injection completely related to  
266 the water contribution. At the same time the reduced testing time allows also assuming constant  
267 values for ionic strength and cation composition. These assumptions hold for the clay-free  
268 materials under study and for limited heating time and may not be completely applicable in the  
269 presence of high concentrations of carbonates.

270 We have now to transform **Eq. [3]** for the purposes of this study, and so to obtain a  
271 relationship between temperature and apparent resistivity variation. By considering  $\sigma_{25}$  as the  
272 reference value at the initial conditions,  $\sigma_T$  the value at a defined step during the test and by  
273 transforming the equation in terms of apparent resistivity we thus obtain:

$$274 \quad \frac{\rho_{a0}}{\rho_{at}} = m(T_t - T_0) + 1 \quad [5]$$

275 where  $\rho_{a0}$  is the apparent resistivity at zero condition (before the starting of the heat injection),  
276  $\rho_{at}$  is the apparent resistivity measured at a defined step,  $T_0$  and  $T_t$  are temperature at the  
277 respective time. From **Eq. [5]** we can obtain:

$$278 \quad \Delta\rho(\%) = \frac{100}{m \Delta T + 1} - 100 \quad [6]$$

279 which relates apparent resistivity variation in percentage  $\Delta\rho_a(\%)$  from zero condition to the  
280 difference in temperature  $\Delta T$ , always depending on the fractional change in resistivity which is  
281 medium-dependent. With **Eq. [6]** we are able to predict the variation in resistivity by knowing  
282 the increase or the decrease in temperature induced in the tested medium. Analogously, by  
283 inverting the proposed relation in terms of temperature it is also possible to predict the  
284 temperature distribution within the medium by performing time-lapse electrical resistivity  
285 measurements, **Eq. [7]**:

$$T_t = \frac{1}{m} \left( \frac{100}{\Delta\rho_\alpha(\%)+100} - 1 \right) + T_0 \quad [7]$$

286  
287 In our approach, we used apparent resistivities avoiding data inversion for several  
288 motivations:

- 289 • given the almost homogeneous condition of the tested materials, measured  
290 apparent resistivities can be quite reasonably approximated to the true resistivity  
291 of the medium;
- 292 • it is well known that inversion can introduce unwanted artifacts that may bias the  
293 results and interpretation particularly on sparse data;
- 294 • the limited number of electrodes (space requirements) and the few measurements  
295 performed did not provide enough data to allow for a rigorous inversion;
- 296 • on a complementary side, few electrodes and short current injection time is  
297 necessary for an acquisition time comparable to the monitored phenomenon and  
298 it is the most common situation in real sites with limited space;
- 299 • last but not least, we wanted to test a fast and simple methodology that could be  
300 potentially applied on site for monitoring purposes, at least in favorable sites (i.e.  
301 characterized by nearly homogeneous conditions), avoiding too much data  
302 elaboration.

303 Apparent resistivities were obtained from measured resistances by adopting a standard  
304 geometric factor ( $k$ ) for dipole - dipole array over infinite homogeneous half-space. To ensure  
305 the reliability of this operation if compared to the limited dimensions of the box, forward model  
306 simulations were carried out with R3t code (Prof. Andrew Binley, © 2012, Lancaster  
307 University), considering the presence of insulating boundaries, in order to estimate  $k$  factor's  
308 differences with respect to homogeneous half-space. Changes in geometrical factor greater than  
309 15% were observed only close to the borders of the box, while divergences in the center are  
310 less than 10% and comparable to measurements' errors (see after). It has moreover to be  
311 considered that data processing was performed with time-lapse differences with respect to  
312 starting conditions; this procedure helps to eliminate the influence of the box's walls on the  
313 apparent resistivity changes observed, being constant the effect on electric current paths during  
314 the tests.

### 315 316 **2.3.2 Data error analysis**

317 As before mentioned, both normal and reciprocal resistance measurements were acquired.  
318 Together with repeatability tests, reciprocal error quantification can be adopted as a measure of  
319 noise in order to prevent misinterpretation of ERT images (Slater et al., 2000). In the present  
320 study, repeatability tests were not performed because as fast as possible resistivity  
321 measurements were needed. Only reciprocal errors were quantified and analyzed in order to  
322 evaluate reliability of the measurements. Reciprocal error known as  $E_{N/R}$  (LaBrecque et al.,  
323 1996) can be achieved by:

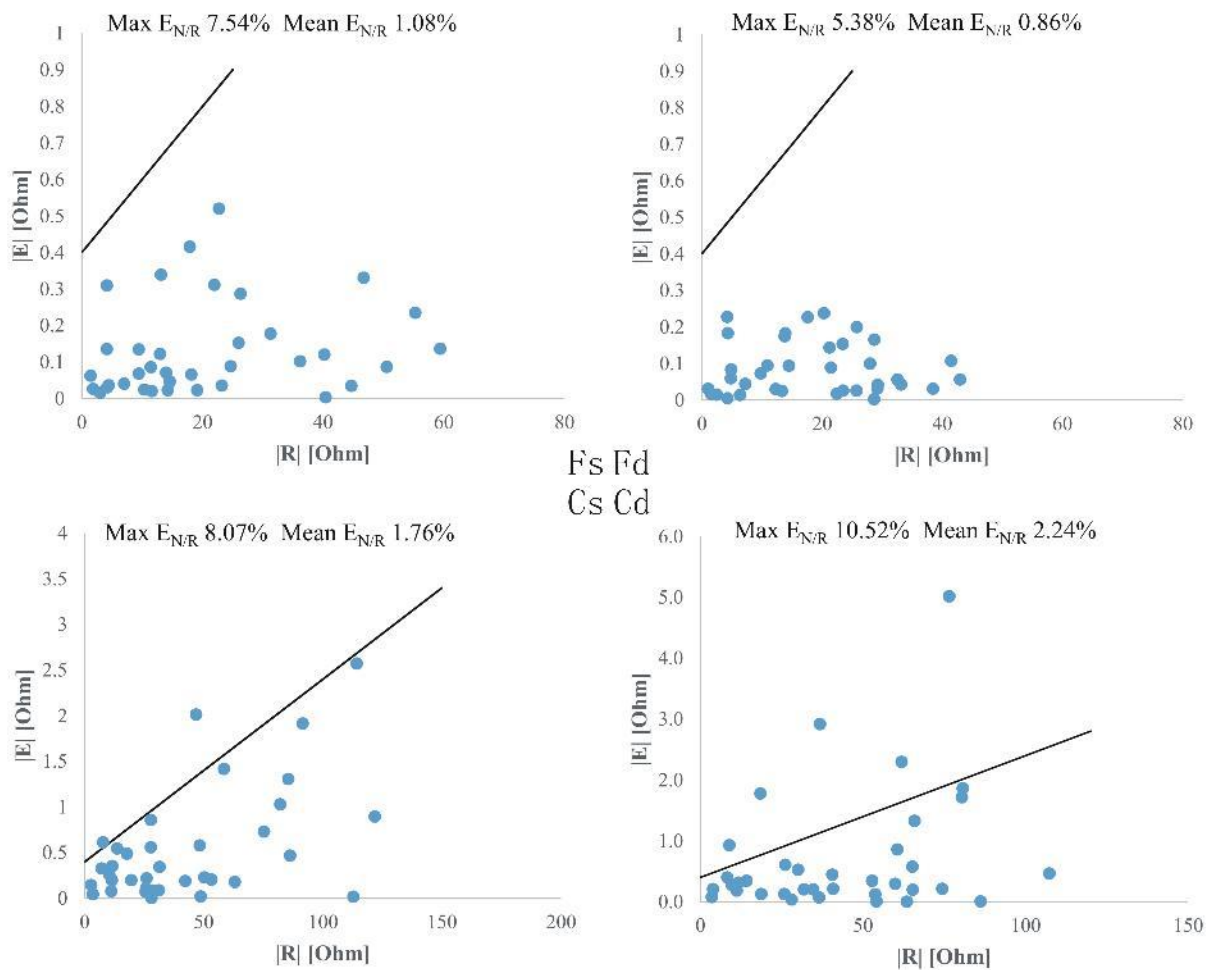
$$324 \quad |E_{N/R}| = R_n - R_r \quad \text{Eq. [8]}$$

325 where  $R_n$  and  $R_r$  are resistances measured by normal and reciprocal quadrupoles respectively.  
326 Since for the principle of reciprocity exchanging current and potential electrodes should not  
327 change measured resistance, reciprocal error gives a measure of data noise.

328  $E_{N/R}$  of each measurement step during heat injection tests were plotted against resistance  
329 data  $R$  (average between normal and reciprocal) and an error envelope given by:

$$330 \quad |E_{N/R}| = a + b \cdot |R| \quad \text{Eq. [9]}$$

331 with  $a = 0.4$  and  $b = 0.02$ , encompassed almost the totality of data in each test. As showed in  
 332 **Fig. 3**, Cd is the worst test, with 6-7 outliers but only 1 of them with error greater than 10%,  
 333 which is typically adopted as threshold (Slater et al., 2000). We therefore decided to keep all  
 334 data sets in each experiment here presented, because even if erasing outliers could bring to  
 335 better apparent resistivity estimation, it is however true that an artificial kriging interpolation  
 336 obtained by voids in the measurements can bring to exaggerated smoothing or artificial imaging  
 337 in the 2D maps. In this case, where only few measurement points are available (owing to above  
 338 mentioned reasons), it was decided to keep all the data but being aware of reciprocal error  
 339 distribution during data interpretation. Again, working with time-lapse differences can lower  
 340 the influence of this error on data processing; indeed, in the performed evaluations  $E_{N/R}$  was  
 341 observed to remain almost constant during the whole duration of the tests.



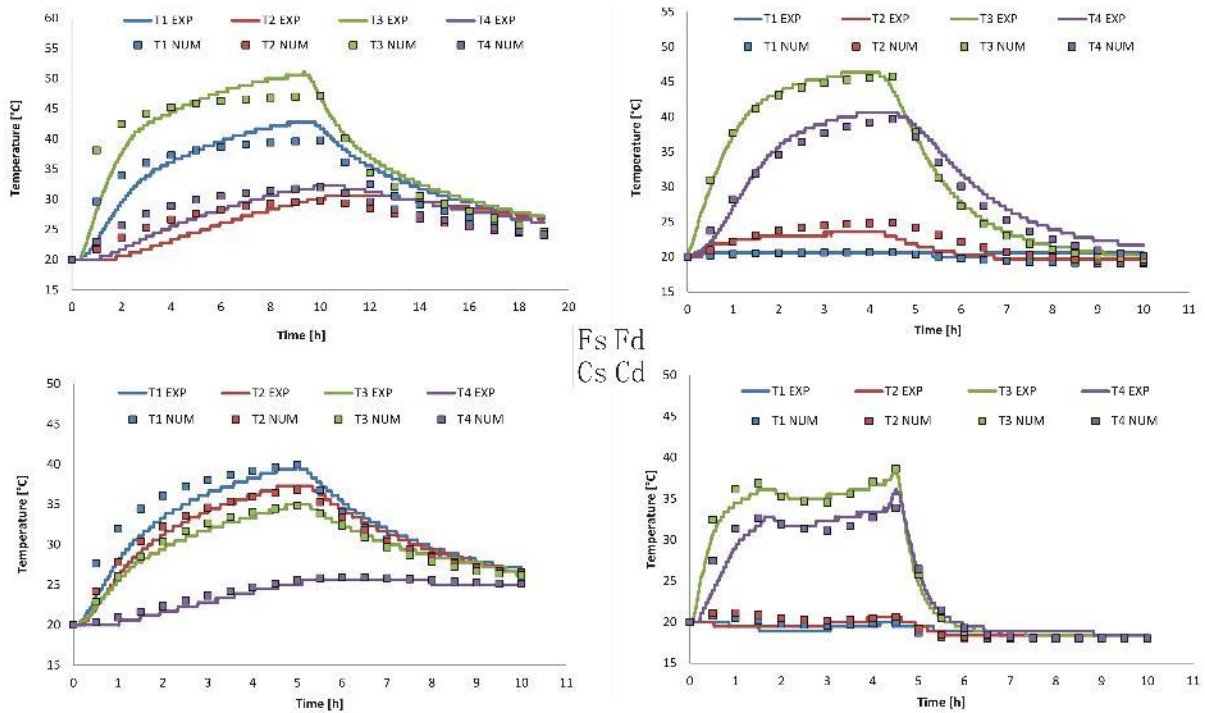
342

343 **Fig. 3.** Reciprocal error  $|E|$  plotted against average resistance values  $|R|$  for the zero condition (before heat  
 344 injection started) of each test. Black lines are the error envelope with  $a = 0.4$  and  $b = 0.02$ . Maximum and mean  
 345 reciprocal errors of each test are also reported.

346

347 **3. RESULTS**

348 The results of the numerical simulations in each of the 4 tests compared with the  
 349 temperature experimental data are reported in **Fig. 4** (for reference to the location of  
 350 temperature sensors refer to **Figs. 6-9**). In **Tab. 3**, the misfit of numerical versus experimental  
 351 temperatures are reported. It can be observed that a valid match was reached in most of the tests  
 352 allowing for the reconstruction of the full temperature field inside the box. Particularly the  
 353 average misfit values remained below 3.5 % for all the tests apart the one under static water  
 354 condition on the fine material (Fs test) which indeed show an increased average uncertainty.  
 355 This test is also the one having the longer injection time causing possible evaporation  
 356 phenomena as will be discussed in section 4.



357  
 358 **Fig. 4.** Comparison between measured (continuous curves) and numerical (dotted curves) temperature data in all  
 359 the tests. In the Fs test, T2 and T1 were 15 and 8 cm upline of the source, while T3 and T4 were downstream at 5  
 360 and 15 cm respectively. For the Fd and Cd tests T1, T2 and T3 were placed at about 10 cm around the source,  
 361 while T4 was at 20 cm. In the Cs test T1, T2 and T3 were placed at 8 from one of the sources, while T4 was at  
 362 20 cm; the OGS numerical simulation also managed to represent the unwanted temperature decrease at the  
 363 source during the Cd test.

364  
 365 **Tab. 3** – Average temperature divergences between numeric and experimental data of Fig. 3 (absolute values in  
 366 %). Steps from 1 to 5 and from 6 to 10 refers respectively to heat up and cool down.

| Test | 1     | 2    | 3    | 4    | 5    | 6    | 7    | 8    | 9    | 10   | Average |
|------|-------|------|------|------|------|------|------|------|------|------|---------|
| Fs   | 13.06 | 7.65 | 4.96 | 4.55 | 1.84 | 7.63 | 9.02 | 8.84 | 9.44 | 9.90 | 7.69    |
| Fd   | 1.61  | 1.86 | 1.96 | 2.59 | 4.36 | 4.39 | 4.88 | 4.05 | 4.68 | 5.47 | 3.59    |
| Cs   | 6.33  | 4.22 | 3.41 | 1.63 | 1.02 | 2.37 | 2.42 | 3.13 | 2.50 | 1.47 | 2.85    |
| Cd   | 6.26  | 2.86 | 3.47 | 1.38 | 3.53 | 2.73 | 3.10 | 2.71 | 2.07 | 2.10 | 3.02    |

367  
 368 The flowing water test on the coarse material (Cd test) showed the smallest peak  
 369 temperature because of the high velocity of the induced flux, which did not allow the water to

370 heat up the medium properly. Contrary to the other ones this test do not present big variations  
 371 between the first and the last hour of the heating period. The hydraulic flux warmed up the  
 372 medium more rapidly, reaching the temperature peak within the first hour. Moreover, after the  
 373 peak, an unexpected temperature decrease in the heat injection during the test (from 60 °C to  
 374 50 °C from hour 1.5 to hour 3) was recorded. This effect was taken into account in the  
 375 simulations. The analogous test in the fine medium is instead characterized by curves shaped  
 376 similarly to stationary tests (Fs and Cs) due to the slower flow velocity. The flux velocity plays  
 377 therefore a major role in transporting the heat. Among all the tests, those performed in the fine  
 378 medium reached the biggest temperature peaks. A finer material is more able to limit the heat  
 379 losses than a coarser one. These losses are mainly ascribable to the pore-filling water, which is  
 380 obviously less constrained by the capillary pressure in a coarser than in a finer medium.

381 **Fig. 5** shows the comparison between the temperature recorded by the 4 sensors during  
 382 the tests (for reference in the location of temperature sensors refer to **Figs. 6-9**) and the  
 383 resistivity-derived temperature obtained by applying **Eq. [7]** to the local resistivity  
 384 measurements nearby the sensors. Best fit  $m$  values of  $0.025\text{ }^{\circ}\text{C}^{-1}$ , for the finer medium, and of  
 385  $0.021\text{ }^{\circ}\text{C}^{-1}$ , for the coarser medium were obtained, reaching again a valid match both in static  
 386 and in dynamic conditions. The temperature-sensitivity of resistivity data is particularly clear  
 387 in the test on the coarse material (Cd test): resistivity data are indeed able to reflect the  
 388 temperature trend during heating related to the decrease in temperature of the source. In the  
 389 cooling periods a divergence between temperature and resistivity-derived data is highlighted in  
 390 Fs and Cd tests. In the first case the resistivity-derived temperature shows a slower return to the  
 391 initial conditions with respect to T-sensor recordings, in the second case the opposite is true. In  
 392 **Tab. 4** the misfit of resistivity-derived versus experimental temperatures are reported. A valid  
 393 agreement can be particularly noted in all the heating periods with an average misfit below 5%.  
 394 In Fs and Cd tests an increase in the average misfit (particularly high for the Cd test) is observed.  
 395 Motivations for this divergence will be discussed in Section 4.

396 **Tab. 4** – Average temperature divergences between resistivity-derived and experimental data of Fig. 4 (absolute  
 397 values in %). Steps from 1 to 5 and from 6 to 10 refers respectively to heat up and cool down.

| Test      | 1     | 2     | 3     | 4     | 5     | 6     | 7     | 8     | 9     | 10    | Average |
|-----------|-------|-------|-------|-------|-------|-------|-------|-------|-------|-------|---------|
| <b>Fs</b> | 7.62  | 4.96  | 4.41  | 4.52  | 4.05  | 1.62  | 4.62  | 6.47  | 8.40  | 9.36  | 5.60    |
| <b>Fd</b> | 3.30  | 3.46  | 3.64  | 3.43  | 5.33  | 7.13  | 3.61  | 2.77  | 3.10  | 2.84  | 3.86    |
| <b>Cs</b> | 5.74  | 2.58  | 1.59  | 1.21  | 1.61  | 2.24  | 2.21  | 4.85  | 3.26  | 4.91  | 3.02    |
| <b>Cd</b> | 11.05 | 13.15 | 13.26 | 11.01 | 11.35 | 20.49 | 20.07 | 23.34 | 23.75 | 24.60 | 17.21   |

398

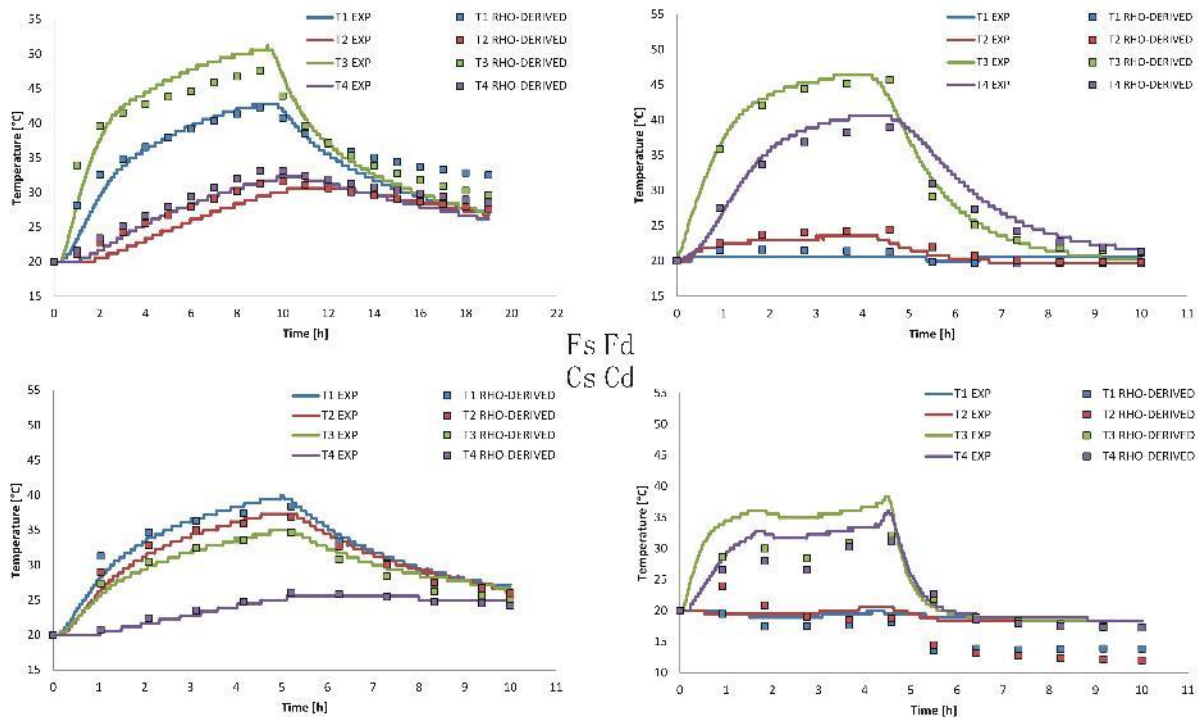
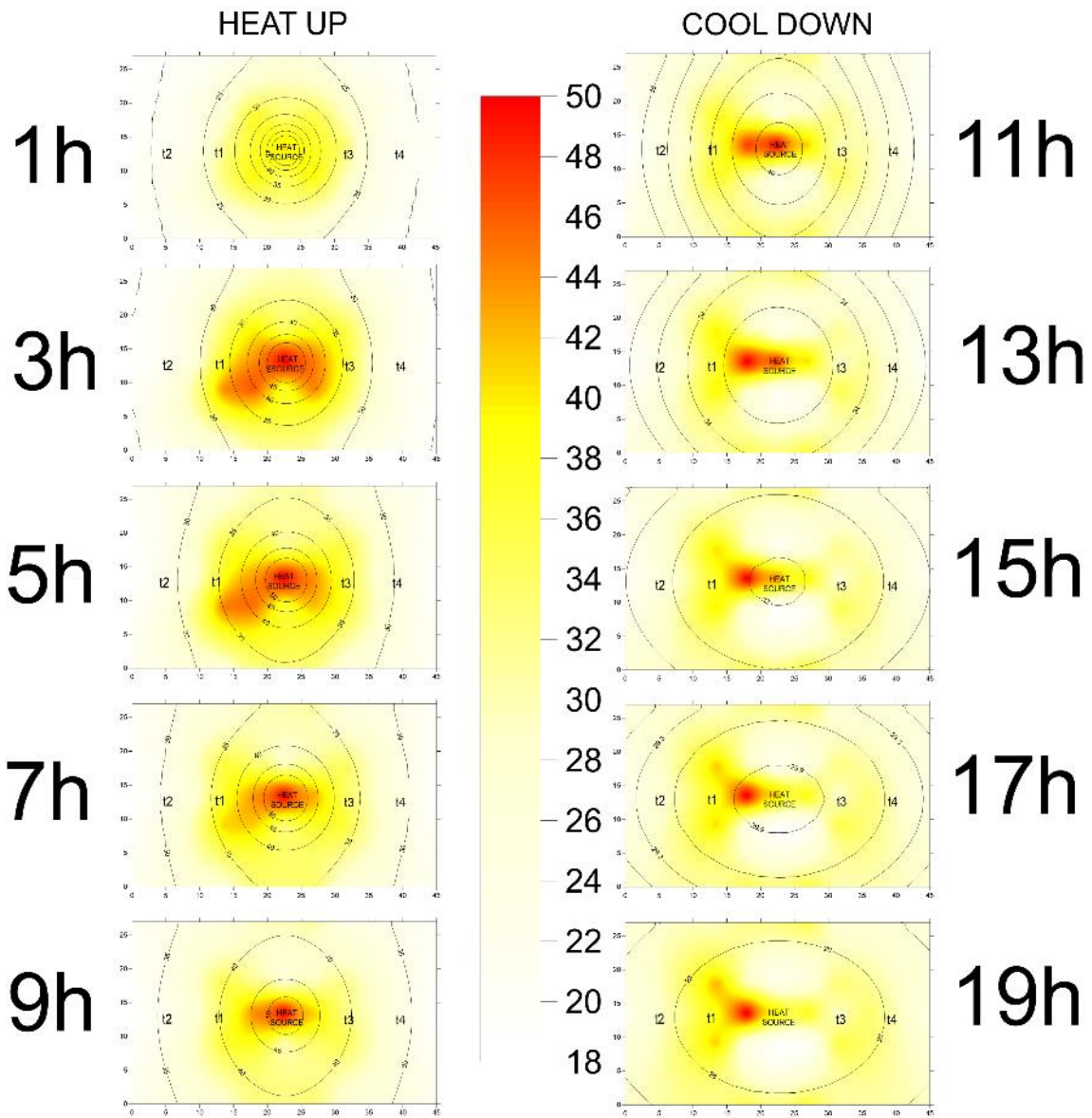


**Fig. 5.** Comparison between measured (continuous curves) and resistivity-derived (dotted curves) temperature data in all the tests. The latter are calculated with Eq. [7] from the resistivity data registered by quadrupoles just around the sensors.

Finally, **Figs. 6, 7, 8** and **9** present the comparison between numerically modelled and resistivity-derived temperatures in all the tests in a 2D representation. These maps were obtained with a Kriging interpolation of the temperature values deduced by apparent resistivity variation. Kriging method was applied accounting for the analysis of the spatial data variability; in each test, best fit of experimental variograms was found to be a linear variogram model in every time step. Apparent resistivity monitoring highlighted its potentiality in describing the heat diffusion from the source in all the tests. In the Fs test (**Fig. 6**), which is the longest among all the performed tests, temperature maps near the peak are not so homogeneous and also the cooling down shows some portions where the resistivity is higher (white portions above and below the source) and other parts where instead a lower resistivity generated a higher temperature estimation. The experiment with flowing water in the fine medium (Fd, **Fig. 7**) shows a good agreement throughout the whole testing time. The left portion of the maps remained at an almost constant temperature for the entire heating period, while the right portion is validly described by the resistivity monitoring, except for some heterogeneities just around the source. The Cs is the best example among all (**Fig. 8**): the heating period is in valid accordance with the peak temperatures and the shape of the heated plume (caused by the presence of two heating sources); the cooling down is also correctly described by the resistivity monitoring. The flowing water test on the coarse material (Cd, **Fig. 9**) shows the ability of the electrical surveys to qualitatively describe the migration of the heated plume due to the water flux. The heating predominant in the right portion of the box is clearly highlighted. The quantitative representation of the temperature field is however not effective as already commented in relation to **Fig. 5**. The discrepancy of the resistivity derived maps from the homogeneous reference condition of numerical simulations (particularly **Figs. 6** and **9**) is however not surprising since probable different effects could be present. Again, motivations for the evidenced discrepancies will be commented in Section 4.

# TEMPERATURE

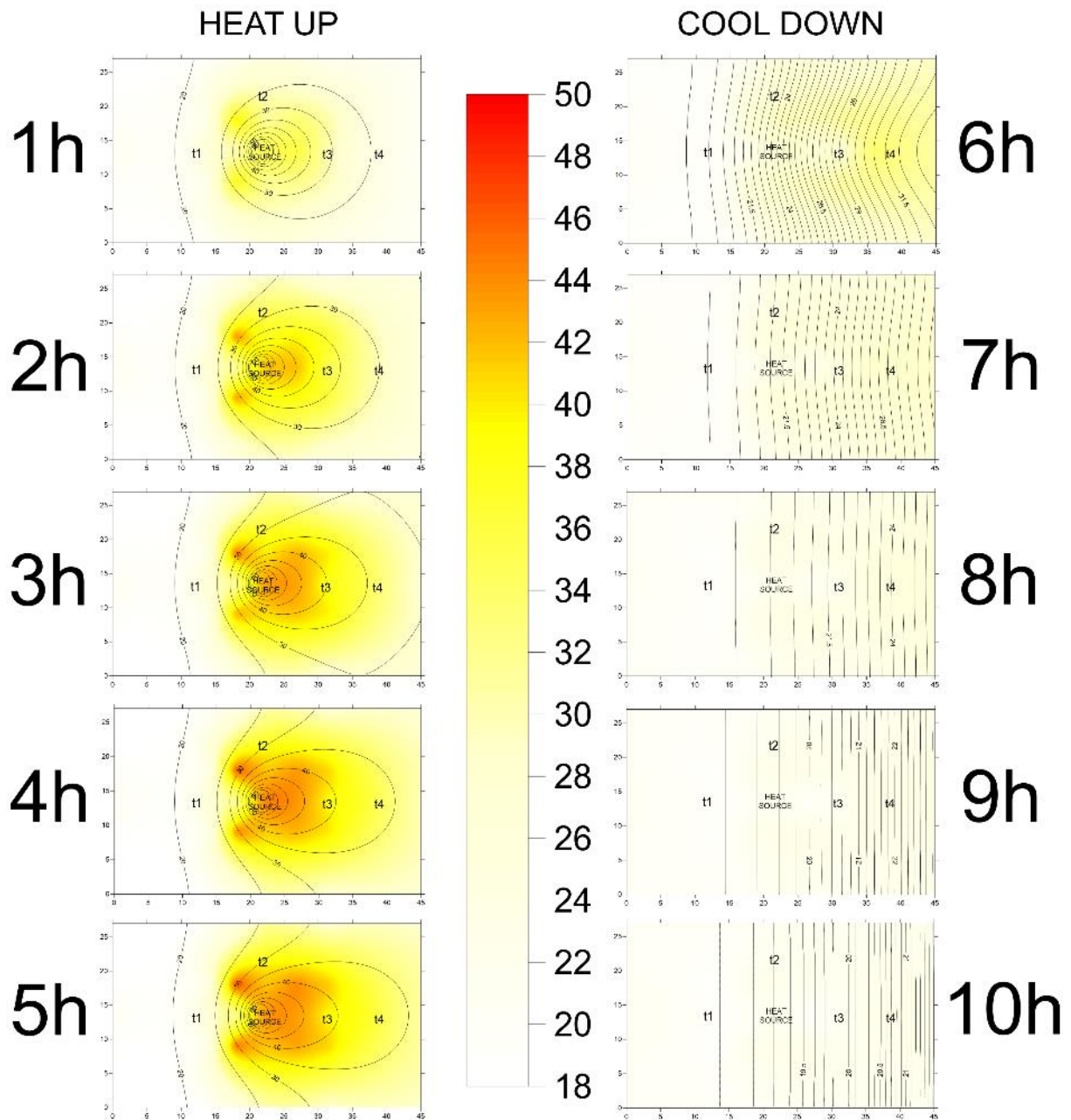


428

429 **Fig. 6.** Comparison between numerical (contours) and resistivity-derived (colored maps) temperature data in the  
430 Fs test. The numerical temperature is provided by the OGS simulation calibrated on the temperature recorded by  
431 each sensor. The resistivity-derived temperature is obtained by Kriging local resistivity transformed data.

432

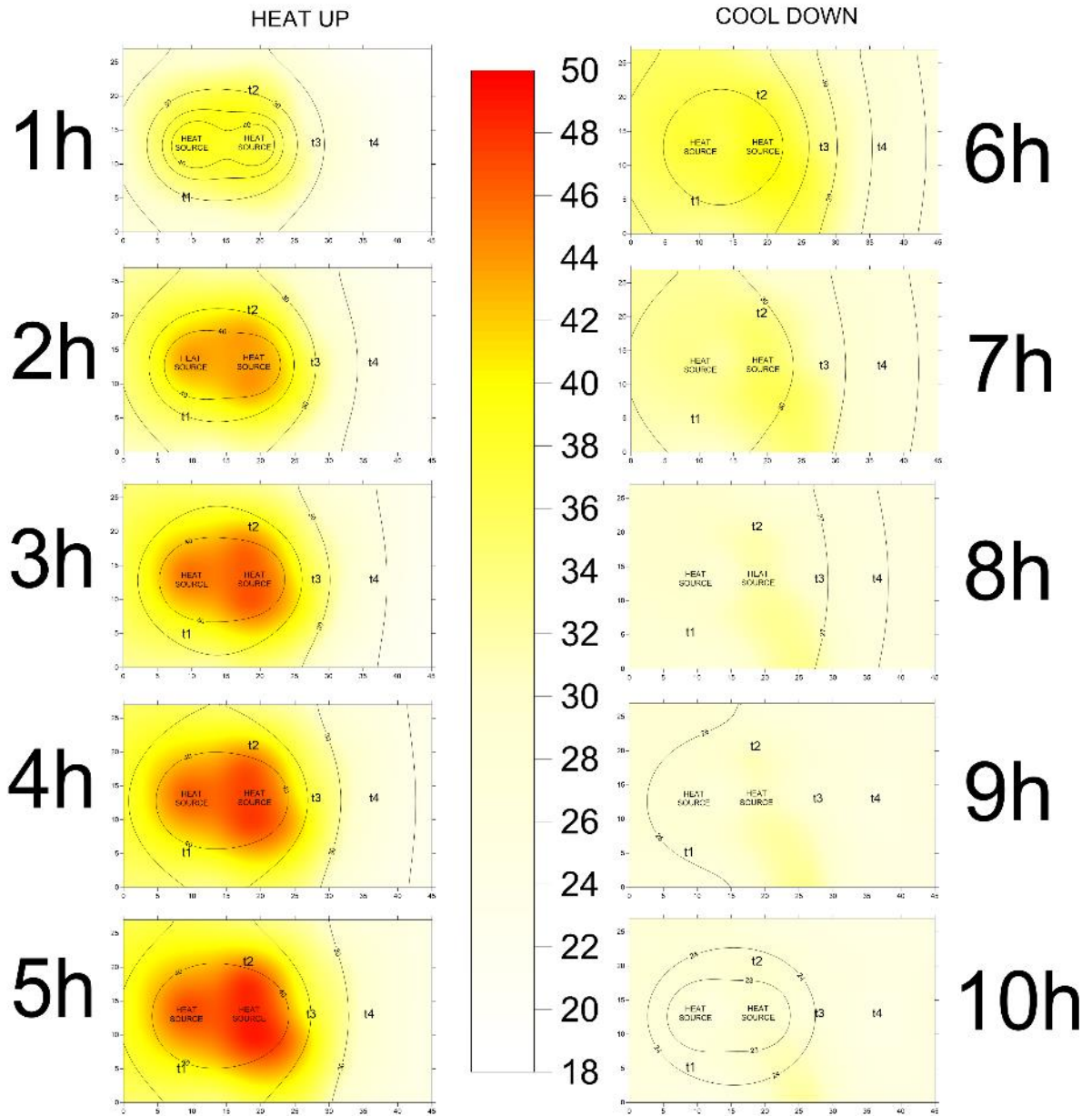
# TEMPERATURE



433  
434  
435  
436  
437

**Fig. 7.** Comparison between numerical (contours) and resistivity-derived (colored maps) temperature data in the Fd test. The numerical temperature is provided by the OGS simulation calibrated on the temperature recorded by each sensor. The resistivity-derived temperature is obtained by Kriging local resistivity transformed data.

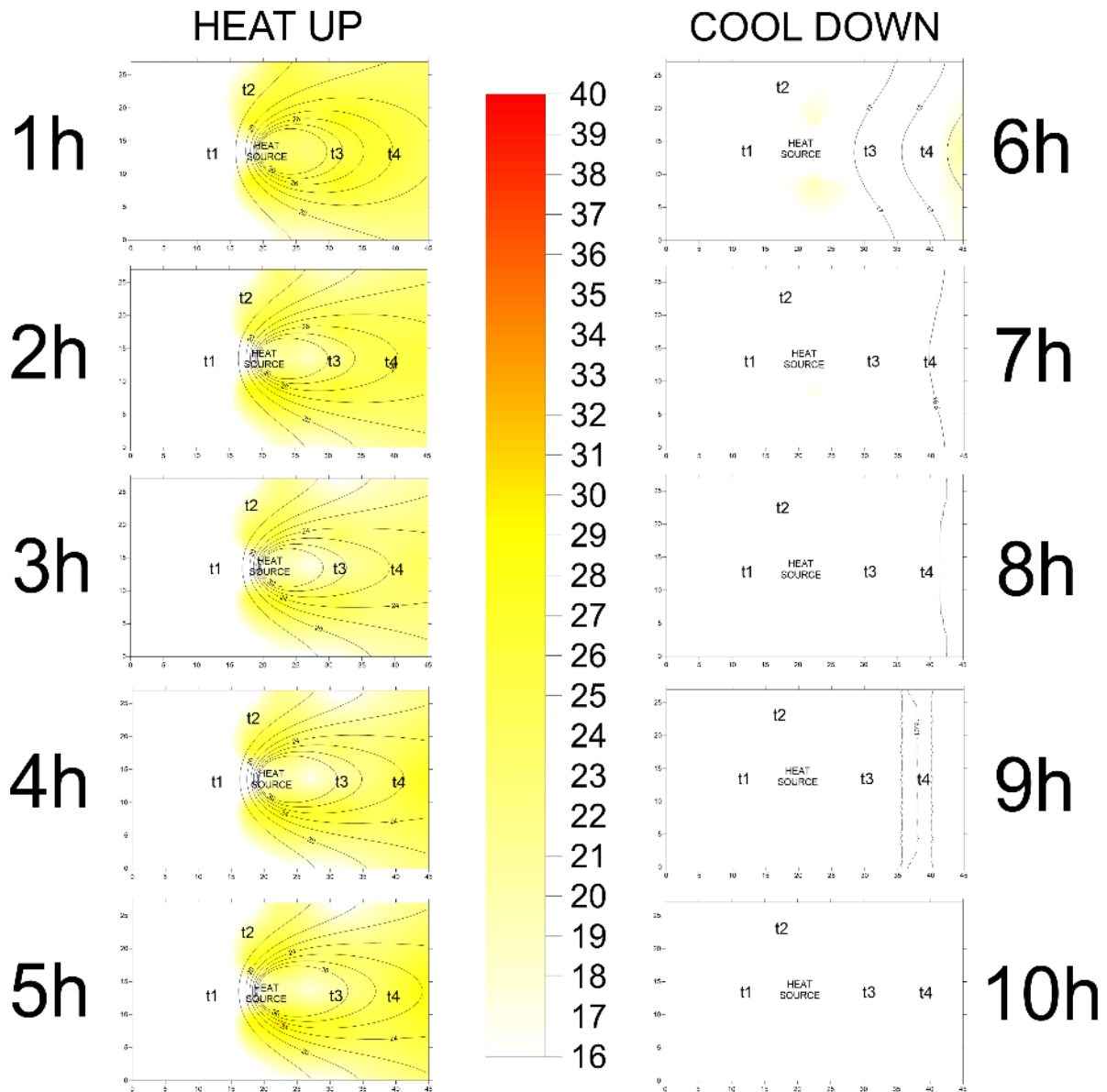
# TEMPERATURE



438  
439  
440  
441  
442

**Fig. 8.** Comparison between numerical (contours) and resistivity-derived (colored maps) temperature data in the Cs test. The numerical temperature is provided by the OGS simulation calibrated on the temperature recorded by each sensor. The resistivity-derived temperature is obtained by Kriging local resistivity transformed data.

# TEMPERATURE



443

444

445

446

447

448

449

450

451

452

453

454

455

456

457

458

**Fig. 9.** Comparison between numerical (contours) and resistivity-derived (colored maps) temperature data in the Cd test. The numerical temperature is provided by the OGS simulation calibrated on the temperature recorded by each sensor. The resistivity-derived temperature is obtained by Kriging local resistivity transformed data.

For quantitatively evaluate the fit of the resistivity estimated temperatures, each resistivity-derived temperature map was compared with the numerical one at each time step. The average of the divergences for each time step is reported in **Tab. 5**. Generally an overestimation trend was always observed. Fs, Fd and Cs tests stand at an acceptable bias of  $10 \pm 2\%$ , while Cd shows worse values, as expected. Among all the tests, in the Cs experiment the best agreement was found, confirming the effective temperature estimate shown in the above reported figures. Conversely to the others, the Cs bias decreases when approaching the peak of the heat injection, reaching the smallest value 1 h after the source's turning off. **Fig. 10** reports a comparison between the numerical and the resistivity-derived TAZ. This can better help in evaluating the potentiality of the resistivity monitoring for imaging the extension of the thermal plume. Fs, Fd and Cs show a valid agreement with a little overestimation particularly in the higher isotherm ( $40^{\circ}\text{C}$ ). Cd test is clearly more disturbed than the others. In general, it can be

459 said that the resistivity measurements performed during the heat injection described the TAZ  
 460 induced in the medium with an acceptable misfit and that the little overestimation of their  
 461 extension can be seen as conservative.

462 **Tab. 5** – Average temperature divergences between numeric and resistivity-derived data of Figs from 5 to 8  
 463 (absolute value in %). Steps from 1 to 5 and from 6 to 10 refers respectively to heat up and cool down.

| Test      | 1     | 2     | 3     | 4     | 5     | 6     | 7     | 8     | 9     | 10    | Average |
|-----------|-------|-------|-------|-------|-------|-------|-------|-------|-------|-------|---------|
| <b>Fs</b> | 9.86  | 11.16 | 12.10 | 14.78 | 13.87 | 10.42 | 11.20 | 12.21 | 13.41 | 14.80 | 12.38   |
| <b>Fd</b> | 10.78 | 11.56 | 11.71 | 11.86 | 12.40 | 7.14  | 6.84  | 6.61  | 7.93  | 7.79  | 9.46    |
| <b>Cs</b> | 10.09 | 7.61  | 7.27  | 7.13  | 7.32  | 6.14  | 6.29  | 6.59  | 8.94  | 12.64 | 8.00    |
| <b>Cd</b> | 25.23 | 26.01 | 28.05 | 29.43 | 29.78 | 28.04 | 37.89 | 39.78 | 41.03 | 41.54 | 32.68   |

464

#### 465 **4. DISCUSSION**

466 The numerical modeling was useful to obtain a reference temperature distribution within  
 467 the medium. The 4 time-lapse local temperature curves registered by the sensors were not  
 468 sufficient alone to interpolate the induced thermal plume throughout the medium This is a  
 469 common problem when local temperature monitoring points are adopted.

470 From a first qualitative look, the results of the electrical surveys showed the expected  
 471 correlation of decreasing electrical resistivity with the increasing temperature induced by the  
 472 heat injection, the opposite is true after the source's turning off. The electrical resistivity  
 473 changed more slowly with increasing distance from the heat source, as temperature did, and  
 474 resulted dependent upon the water flux conditions within the material. As an average between  
 475 all the performed tests (both fine and coarse medium), it was observed that a 10% positive  
 476 variation in temperature generates a 2% – 3% negative change in electrical resistivity.  
 477 Generally, the heating periods were appreciably monitored by resistivity measurements and the  
 478 resistivity-derived temperatures are in valid accordance with the numerical model. Conversely,  
 479 in the cooling periods a slight divergence between temperature and resistivity-derived data is  
 480 particularly highlighted in Fs and Cd tests (**Fig. 5**), same divergences are also partially noticed  
 481 in the comparison of temperature and numerical curves (**Fig. 4**). At the same time some  
 482 heterogeneities appears in some of the presented resistivity-derived temperature maps  
 483 (particularly in Fs and Cd tests, **Fig. 6** and **9**). These can be related to different phenomena  
 484 occurring in the medium: (i) evaporation, (ii) chemical reactions induced in the water and (iii)  
 485 velocity of the water flux.

- 486 (i) Evaporation process seems to disturb only when a prolonged heat injection is performed.  
 487 The resistivity measurements were indeed mainly disturbed in the Fs test, in which a 9 h  
 488 heat injection was performed, while they were not influenced in other experiments.  
 489 Evaporation processes, observed on the surface of the box, caused a fictitious increase in  
 490 resistivity which is not related to the temperature dependence, so that heterogeneities may  
 491 occur in temperature visualization (**Fig. 6**) and anomalies in the resistivity derived  
 492 temperature curves (**Fig. 5**). The evaporation process has been quantified by local direct  
 493 measurements at the end of the test showing a reduction of about 10% water content in a  
 494 10 cm zone around the source. This reflect in a more remarkable temperature difference  
 495 for the sensors located near the source (T1 and T3) than for the farthest ones (T2 and T4).  
 496 Since the temperature estimation from resistivity data is based on a measured resistivity  
 497 difference this effect could cause both a lower estimated temperature at the peak and an  
 498 higher estimated temperature in cool down.

499 (ii) During the cool down of the same test, data show a return to slightly lower resistivity in  
500 respect to the initial condition (higher apparent temperature). This can be attributed to  
501 chemical reactions' effect (e.g. mineral dissolution processes occurred in the medium  
502 during the heating up). We can hypothesize that the heat injection produces an increase  
503 in water TDS (total dissolved solids) that lowers the bulk medium resistivity. As for  
504 evaporation, chemical reactions' problem only occurs when a prolonged heat injection is  
505 performed; no bias related to this issue is highlighted in other tests. A quantification of  
506 this effect was indeed performed during the Fs and Fd tests by measuring fluid resistivity.  
507 In Fs test, a value of  $22.3 \pm 0.1 \Omega \text{ m}$  was measured in the water squeezed from a sample  
508 at the end of the test. Conversely, in the Fd test a value of  $22.8 \pm 0.1 \Omega \text{ m}$  was constantly  
509 monitored in the water going out of the box after passing through the medium. The initial  
510 water resistivity was  $22.7 \Omega \text{ m}$  in both tests. This means that during the conduction +  
511 convection test (Fd) no relevant water resistivity variation due to changes in TDS was  
512 observed, while an only slight reduction was noted in the pure conduction test (Fs)  
513 partially responsible, together with evaporation, of worse data fit. It must be also  
514 underlined that the above mentioned water resistivity values were estimated on the whole  
515 water volume within the box, smearing possible localized anomalies. It is thus possible  
516 that, in limited zones nearby the source, mineral dissolution effect could be more relevant.  
517 Generally, we can however say that more specific analyses are necessary in order to  
518 evaluate and discern evaporation and chemical reactions influences on resistivity  
519 measurements. Divergences here highlighted between registered and resistivity-derived  
520 temperatures can be of course related to the action of both processes together.

521 (iii) Flux velocity, higher in the Cd test, provided worse resistivity-derived temperatures (**Fig.**  
522 **5**). The rapid change of the flowing water within the box did not allow the heat injection  
523 to change the water resistivity in the medium's portions located upstream of the source.  
524 Moreover, a slightly higher resistivity is observed after source's turning off, showing a  
525 cool down due to the lower temperature of the water flow. The difference of the 2D  
526 temperature maps (numerical and resistivity-derived) in this test (**Fig. 10**) also underlines  
527 that localized flow paths could be present in the coarser material. These are not reflected  
528 in the numerical simulation, which assumes an homogeneous medium, but they are  
529 underlined in the resistivity measurements. In the Fd test, in which the flux is slower, heat  
530 injection is able to change water resistivity, so the two results are in better agreement. It  
531 can be said that resistivity-derived temperature are reliable in the dynamic test with low  
532 flux velocity, while they are less trustworthy when a high flux velocity is provided.



538 **4. CONCLUSIONS**

539 The present paper presented a series of tests carried out on a laboratory device, build for  
540 testing and calibrating the use of electrical apparent resistivity measurements for monitoring  
541 the thermal affected zone caused by heat injection. Four examples among the several performed  
542 tests were presented. Hourly apparent resistivity measurements were performed on two  
543 different porous media in order to image the temperature field within the box. The methodology  
544 was supported by numerical simulations calibrated on the temperature recorded by the sensors.

545 The outcomes of the tests highlighted the reliability of the time-lapse electrical  
546 measurements for qualitatively predicting the heat propagation within saturated porous media.  
547 The tests showed an acceptable agreement between the TAZ extensions extracted from different  
548 approaches (e.g. direct temperature measurements, numerical simulations and apparent  
549 resistivity measurements). Radial heat diffusion from the heat source was well described by the  
550 variation of apparent resistivity data in tests without flowing water. Tests under flowing water  
551 conditions underlined the disturbance of the water flux on the electrical resistivity  
552 measurements; the faster the flux velocity, the higher the interference in the collected data.  
553 Resistivity measurements appears to reveal more details then simple thermal or thermo-  
554 hydraulic modeling. Further studies are however necessary for completely understanding the  
555 eventual influence of chemical reactions which occur in a porous medium when a heat injection  
556 is provided, particularly at laboratory scale. This could provide a better calibration of resistivity-  
557 derived curves in order to be applicable also in field testing.

558 This study was precursor to what we are planning to do on a living lab prepared at the  
559 campus of Torino University in Grugliasco (Giordano et al., 2016; GTES, 2014), where a small  
560 ground heat storage system was built. The purpose of this living lab is to replicate at the field  
561 scale the laboratory experiments here presented and to serve as a model for further concrete  
562 developments of energy saving applications in northern Italy.

563

564 **REFERENCES**

- 565 Arato, A., Boaga, J., Comina, C., De Seta, M., Di Sipio, E., Galgaro, A., Giordano, N., Mandrone, G., 2015.  
 566 Geophysical monitoring for shallow geothermal applications – two Italian case histories. *First Break – Near*  
 567 *Surface Geoscience* 33(8), 75-79.
- 568 Arslan, U., Huber H., 2013. Numerical back-analyses of laboratory tests with forced groundwater flow.  
 569 *Proceedings of the Thirty-Eighth Workshop on Geothermal Reservoir Engineering*, 1-5.
- 570 Bakema, G., Snijders, A.L., Nordell, B., 1995. *Underground Thermal Energy Storage, State of the Art Report*  
 571 1994. Arnhem, The Netherlands, 83 pp.
- 572 Bolève, A., Crespy, A., Revil, A., Janod, F., Mattiuzzo, J.L., 2007. Streaming potentials of granular media:  
 573 Influence of the Duhkin and Reynolds numbers. *Journal of Geophysical Research* 112, B08204, doi:  
 574 10.1029/2006JB004673.
- 575 Bonte, M., 2013. Impacts of shallow geothermal energy on groundwater quality: A hydrochemical and  
 576 geomicrobial study of the effects of ground source heat pumps and aquifer thermal energy storage. Phd Thesis,  
 577 Gildeprint Enschede, ISBN 978-94-6108-544-3, 175 pp.
- 578 Campbell, R.B., Bower, C.A., Richard, L.A., 1948. Change in electrical conductivity with temperature and the  
 579 relation with osmotic pressure to electrical conductivity and ion concentration for soil extracts. *Soil Science*  
 580 *Society of America Proceedings* 13, 33-69.
- 581 Dickinson, J.S., Buik, N., Matthews, M.C., Snijders, A., 2009. Aquifer thermal energy storage: theoretical and  
 582 operational analysis. *Geotechnique* 59, 249-260.
- 583 Fisch, M.N., Guigas, M., Dalenbäck, J.O., 1998. A review of large-scale solar heating systems in Europe. *Solar*  
 584 *Energy* 63(6), 355-366.
- 585 Fragkogiannis, G., Papatheodorou, N., Stamataki, S., 2008. Evaluation of Thermal Performance of Ground -  
 586 Source Energy Systems. A geophysics supported approach. *World Renewable Energy Congress X and Exhibition*,  
 587 July 19<sup>th</sup>-25<sup>th</sup>, Glasgow, Scotland.
- 588 Friedman, S. P., 2005. Soil properties influencing apparent electrical conductivity: a review. *Computers and*  
 589 *Electronics in Agriculture* 46, 45-70.
- 590 Giordano, N., Comina, C., Mandrone, G., Cagni, A., 2016. Borehole thermal energy storage (BTES). First results  
 591 from the injection phase of a living lab in Torino (NW Italy). *Renewable Energy* 86, 993-1008, doi:  
 592 10.1016/j.renene.2015.08.052.
- 593 Hayashi, M., 2004. Temperature-electrical conductivity relation of water for environmental monitoring and  
 594 geophysical data inversion. *Environmental Monitoring and Assessment* 96, 119-128, doi:  
 595 10.1023/B:EMAS.0000031719.83065.68.
- 596 Hayley, K., Bentley, L.R., Gharibi, M., Nightingale, M., 2007. Low temperature dependence of electrical  
 597 resistivity: Implications for near surface geophysical monitoring. *Geophysical Research Letters* 34, L18402, doi:  
 598 10.1029/2007GL031124.
- 599 Hermans, T., Vandenbohede, A., Lebbe, L., Nguyen, F., 2012. A shallow geothermal experiment in a sandy aquifer  
 600 monitored using electric resistivity tomography. *Geophysics* 77(1), B11-B21.
- 601 Hermans, T., Nguyen, F., Robert, T., Revil, A., 2014. Geophysical methods for monitoring temperature changes  
 602 in shallow low enthalpy geothermal systems. *Energies* 7, 5083-5118, doi: 10.3390/en7085083.
- 603 Hermans, T., Wildemeersch, S., Jamin, P., Urban, P., Brouyère, S., Dassargues, A., Nguyen, F., 2015. Quantitative  
 604 temperature monitoring of a heat tracing experiment using cross-borehole ERT. *Geothermics* 53, 14-26.
- 605 Kolditz, O., Bauer, S., Bilke, L., Böttcher, N., Delfs, J.O., Fischer, T., Görke, U.J., Kalbacher, T., Kosakowski,  
 606 G., McDermott, C.I., Park, C.H., Radu, F., Rink, K., Shao, H.B., Sun, F., Sun, Y.Y., Singh, A.K., Taron, J.,  
 607 Walther, M., Wang, W., Watanabe, N., Wu, Y., Xie, M., Xu, W., Zehner, B., 2012. OpenGeoSys: an opensource  
 608 initiative for numerical simulation of thermo-hydro-mechanical/chemical (THM/C) processes in porous media,  
 609 *Environmental Earth Science* 67, 589-599.
- 610 LaBrecque, D.J., Miletto, M., Daily, W., Ramirez, A., Owen, E., 1996. The effects of noise on Occam's inversion  
 611 of resistivity tomography data. *Geophysics* 61, 538-548.

- 612 Lee, Y., Deming, D., 1998. Evaluation of thermal conductivity temperature corrections applied in terrestrial heat  
613 flow studies. *Journal of Geophysical Research* 103(B2), 2447-2454.
- 614 Lo Russo, S., Gnani, L., Rocca, E., Taddia, G., Verda, V., 2014. Groundwater Heat Pump (GWHP) system  
615 modeling and Thermal Affected Zone (TAZ) prediction reliability: Influence of temporal variations in flow  
616 discharge and injection temperature. *Geothermics* 51, 103-112.
- 617 Loke, M.H., 2000. *Electrical imaging surveys for environmental and engineering studies – A practical guide to 2-  
618 D and 3-D surveys.* Copyright (1999) M.H. Loke, 67 pp.
- 619 Novo, A.V., Bayon, J.R., Castro-Fresno, D., Rodriguez-Hernandez, J., 2010. Review of seasonal heat storage in  
620 large basins: Water tanks and gravel-water pits. *Applied Energy* 87, 390-397.
- 621 Paskoy, H.O., Andersson O., Abaci, S., Evliya, H., Turgut, B., 2000. Heating and cooling of a hospital using solar  
622 energy coupled with seasonal thermal energy storage in an aquifer. *Renewable Energy* 19, 117-122.
- 623 Rein, A., Hoffman, R., Dietrich, P., 2004. Influence of natural time-dependent variations of electrical conductivity  
624 on DC resistivity measurements. *Journal of Hydrology* 285, 215-232.
- 625 Reuss, M., Beuth, W., Schmidt, M., Schoelkopf, W., 2006. Solar district heating with seasonal storage in  
626 Attenkirchen. ECOSTOCK 2006, in: 10th International Conference on Thermal Energy Storage, Stockton, USA.
- 627 Revil, A., Cathles, L.M., Losh, S., Nunn, J.A., 1998. Electrical conductivity in shaly sands with geophysical  
628 applications. *Journal of Geophysical Research* 103, 23925-23936, doi: 10.1029/98JB02125.
- 629 Revil, A., Linde, N., 2006. Chemico-electrochemical coupling in micro-porous media. *Journal of Colloid and  
630 Interface Science* 302, 682-694, doi: 10.1016/j.jcis.2006.06.051.
- 631 Robert, T., Hermans, T., Dumont, G., Nguyen, F., Rwabuhungu, D.E., 2013. Reliability of ERT-derived  
632 temperature – Insights from laboratory measurements. Near Surface Geoscience, Proceedings of 19<sup>th</sup> European  
633 Meeting of Environmental and Engineering Geophysics, TuS2a10, Bochum, Germany, 9-11 September 2013.
- 634 Rosen, M.A., 1999. Second-law analysis of aquifer thermal energy storage systems. *Energy* 24, 167-182.
- 635 Sanner, B., Karytsas, C., Mendrinou, D., Rybach, L., 2003. Current status of ground source heat pumps and  
636 underground thermal energy storage in Europe. *Geothermics* 32, 579-588.
- 637 Schmidt, T., Mangold, D., Müller-Steinhagen, H., 2004. Central solar heating plants with seasonal storage in  
638 Germany. *Solar Energy* 76, 165-74.
- 639 Slater, L., Binley, A.M., Daily, W., Johnson, R., 2000. Cross-hole electrical imaging of a controlled saline tracer  
640 injection. *Journal of Applied Geophysics* 44, 85-102.
- 641 Xu, J., Wang, R.Z., Li, Y., 2014. A review of available technologies for seasonal thermal energy storage. *Solar  
642 Energy*, 103: 610-638.

#### 643 **WEB REFERENCES**

- 644 DLSC - Drake Landing Solar Community, 2012. Borehole thermal energy storage (BTES) - <http://dlsc.ca> accessed  
645 on September 21
- 646 GTES Grugliasco Living Lab, 2014 – [www.gtes.unito.it](http://www.gtes.unito.it) accessed 2015 September 21.
- 647 Prof. Andrew Binley, © 2012, Lancaster University - [www.es.lancs.ac.uk/people/amb/Freeware/R3t/R3t.htm](http://www.es.lancs.ac.uk/people/amb/Freeware/R3t/R3t.htm)  
648 accessed on 2015 September 21.